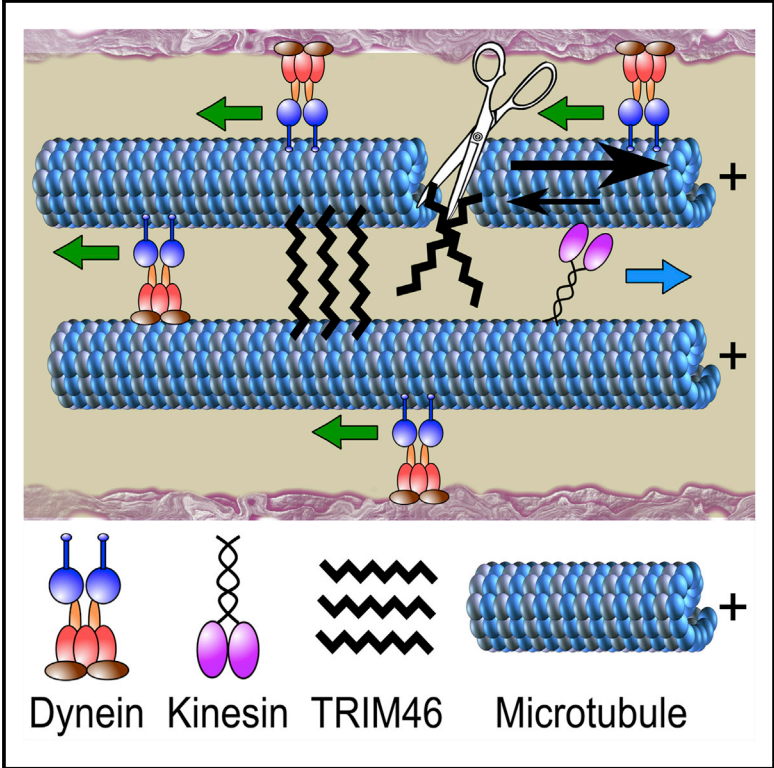


Cell Reports

Cytoplasmic Dynein Transports Axonal Microtubules in a Polarity-Sorting Manner

Graphical Abstract



Authors

Anand N. Rao, Ankita Patil, Mark M. Black, Erin M. Craig, Kenneth A. Myers, Howard T. Yeung, Peter W. Baas

Correspondence

pbaas@drexelmed.edu

In Brief

Rao et al. show that the plus-end-out microtubule polarity pattern of the axon can be explained by a polarity-sorting mechanism driven by cytoplasmic dynein, together with the participation of other players that include an opposing motor and a cross-linker protein.

Highlights

- Cytoplasmic dynein transports microtubules bi-directionally in the axon
- Dynein-based transport sorts microtubules according to their polarity orientation
- Computational modeling predicts other molecular players as well as dynein
- TRIM46 acts as a cross-linker that influences microtubule transport



Cytoplasmic Dynein Transports Axonal Microtubules in a Polarity-Sorting Manner

Anand N. Rao,¹ Ankita Patil,¹ Mark M. Black,² Erin M. Craig,³ Kenneth A. Myers,⁴ Howard T. Yeung,³ and Peter W. Baas^{1,5,*}

¹Department of Neurobiology and Anatomy, Drexel University, Philadelphia, PA 19129, USA

²Department of Anatomy and Cell Biology, Temple University, Philadelphia, PA 19140, USA

³Department of Physics, Central Washington University, Ellensburg, WA 98926, USA

⁴Department Biological Sciences, University of the Sciences, Philadelphia, PA 19104, USA

⁵Lead Contact

*Correspondence: pbaas@drexelmed.edu

<http://dx.doi.org/10.1016/j.celrep.2017.05.064>

SUMMARY

Axonal microtubules are predominantly organized into a plus-end-out pattern. Here, we tested both experimentally and with computational modeling whether a motor-based polarity-sorting mechanism can explain this microtubule pattern. The posited mechanism centers on cytoplasmic dynein transporting plus-end-out and minus-end-out microtubules into and out of the axon, respectively. When cytoplasmic dynein was acutely inhibited, the bi-directional transport of microtubules in the axon was disrupted in both directions, after which minus-end-out microtubules accumulated in the axon over time. Computational modeling revealed that dynein-mediated transport of microtubules can establish and preserve a predominantly plus-end-out microtubule pattern as per the details of the experimental findings, but only if a kinesin motor and a static cross-linker protein are also at play. Consistent with the predictions of the model, partial depletion of TRIM46, a protein that cross-links axonal microtubules in a manner that influences their polarity orientation, leads to an increase in microtubule transport.

INTRODUCTION

Axonal microtubules (MTs) are nearly uniformly oriented with a plus-end-out pattern (Heidemann et al., 1981), but a small number are minus-end-out, especially during development (Hasaka et al., 2004; Yau et al., 2014). This MT polarity pattern is preserved by limiting MT assembly either to existing MTs (Baas and Ahmad, 1992) or to nucleation of MTs of the same orientation from the sides of existing MTs (Sánchez-Huertas et al., 2016). Minus-end-out MTs can arise during bouts of MT severing that occur during plastic events such as branch formation, because the very shortest MTs can flip orientation (Qiang et al., 2010). A potential mechanism for organizing axonal MTs called “polarity sorting” is based on in vitro observations that a lawn of motor proteins adhered to a glass coverslip transport

(or “slide”) apart MTs of opposite orientation. The motor protein adheres to the glass via its cargo domain, leaving the motor domain available to swivel so that it transports MTs in a polarity-sorting manner (Tanenbaum et al., 2013). Such a mechanism in the axon would not only transport MTs into the axon with plus ends leading but would also correct for MT polarity flaws by transporting minus-end-out MTs back to the cell body.

Cytoplasmic dynein is a good candidate for the relevant motor protein because it transports MTs with plus ends leading (Dillman et al., 1996; Ahmad et al., 1998). However, in apparent contradiction with this possibility, gradual depletion of dynein heavy chain (DHC) from cultured rat neurons from the superior cervical ganglion (SCG) resulted in diminution of the anterograde, but not retrograde, transport of axonal MTs (He et al., 2005). This may be because gradual depletion of DHC provides the opportunity for other motors to aberrantly transport MTs (Baas and Mozgova, 2012; Arthur et al., 2015; Zheng et al., 2008). Here, we used various methods, including an acute approach to test dynein’s potential role in polarity-sorting axonal MTs, and then used computational modeling to ascertain whether the data can be explained by dynein-based polarity sorting of MTs.

RESULTS

Ciliobrevin D Acutely and Reversibly Inhibits Dynein Function in Rat Neurons

Ciliobrevin D (CB), a drug that acts in a nucleotide-competitive manner to acutely and specifically inhibit the ATPase activity of cytoplasmic dynein (Firestone et al., 2012), has been used in recent studies on cultured neurons (Roossien et al., 2014; Sainath and Gallo, 2015). An advantage of CB not shared by previous methods of dynein inhibition is that CB is reversible upon washout, providing a method to re-introduce dynein function after acute or prolonged inhibition. Treatment of SCG cultures with CB led to Golgi dispersion at concentrations of 50 μ M and 100 μ M, with a 56% \pm 4% and 77% \pm 7% increase in cells displaying dispersed Golgi, respectively. CB washout rescued neurons from the dispersed Golgi phenotype, reducing the number of cells with dispersed Golgi to near-control levels (Figures 1A and 1B). Neurons treated with CB showed significantly fewer ($p < 0.01$) filopodia occupied by MTs when compared to untreated and

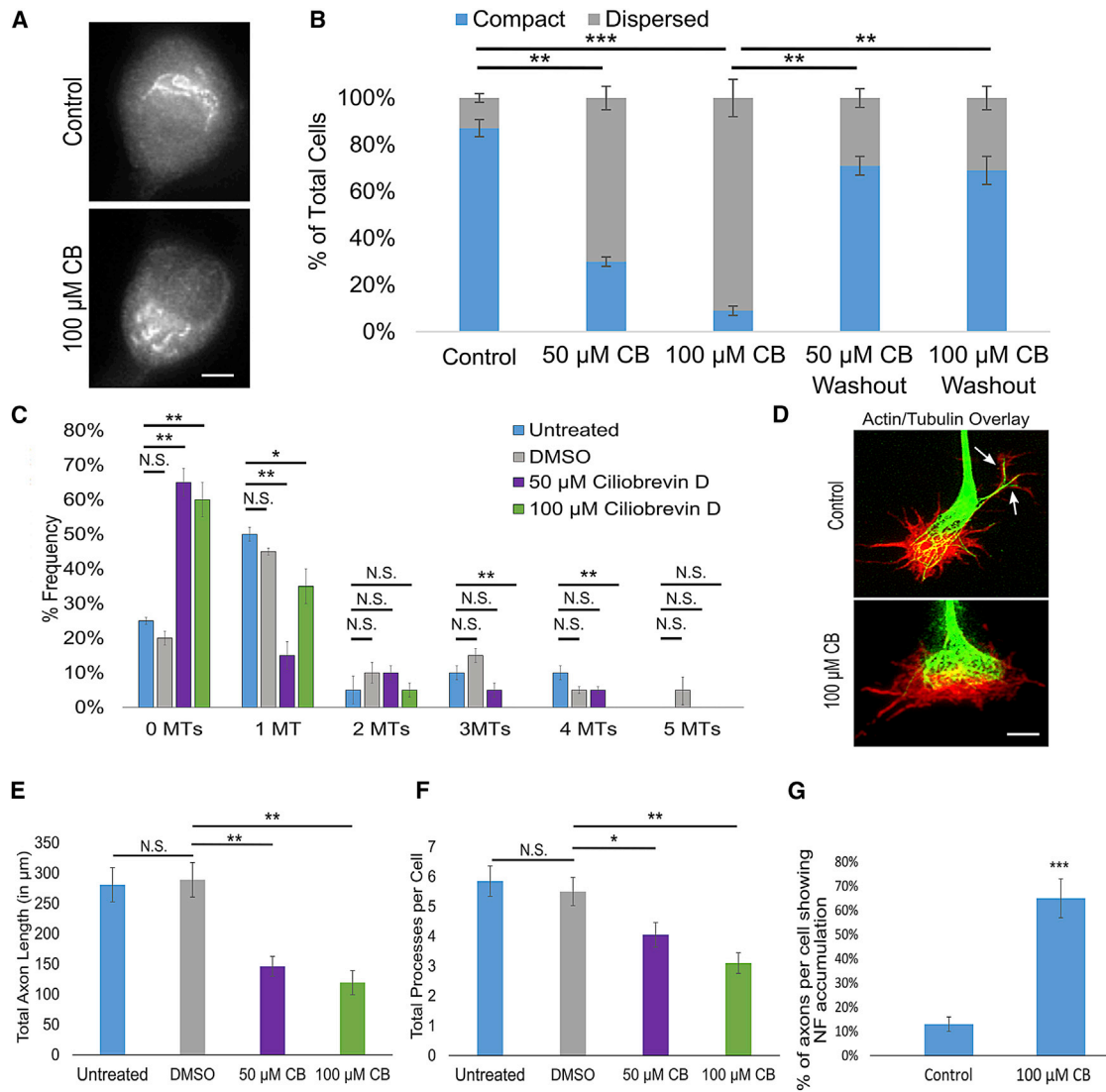


Figure 1. CB Inhibits Dynein Specifically and Reversibly in Rat SCG Neurons

(A) Golgi immunostaining with CB or vehicle (scale bar, 5 μm). (B) Bar graph showing the percentage of cells with dispersed Golgi, with vehicle, CB, and CB washout at two different concentrations. (C) Frequency histogram of the number per growth cone of filopodia-containing MTs after treatment with CB versus control. (D) Actin and tubulin immunostaining of neuronal growth cones after treatment with CB or vehicle (scale bar, 2 μm). (E) Bar graph depicting total axon length under various conditions. (F) Bar graph showing total processes per cell under various conditions. (G) Bar graph of the percentage of axons per cell showing neurofilament (NF) accumulation after treatment with CB or vehicle. n = 50 neurons per condition from three independent dissections. Data represent mean ± SEM. *p < 0.05; **p < 0.01; ***p < 0.001. N.S., not significant.

vehicle-control neurons (DMSO), with the number of filopodia not occupied by a MT jumping from roughly 20% to over 60% and significantly fewer growth cones containing one or more MTs (Figures 1C and 1D). CB-treated neurons displayed reduced total axon length and process number per cell (Figures 1E and 1F), with an increased percentage of cells showing neurofilament accumulation in axon tips (Figure 1G). Finally, CB treatment suppressed retrograde transport of fluorescently conjugated dextrans (vesicle transport) 15 min after CB wash-in (Figure S1A). All of these observations are consistent with expectations of dynein in-

hibition, with an even greater preference for inhibition of vesicle transport in the retrograde direction than observed with gradual depletion of DHC by small interfering RNA (siRNA) (Myers et al., 2006; Ahmad et al., 2006; He et al., 2005).

Dynein Inhibition Alters MT Polarity Orientation in the Axon and Reintroduction of Dynein Rescues the Altered MT Phenotype

MT polarity orientation was assessed with GFP-EB3 at 3, 24, and 48 hr after plating with no treatment or in the presence of 50 or

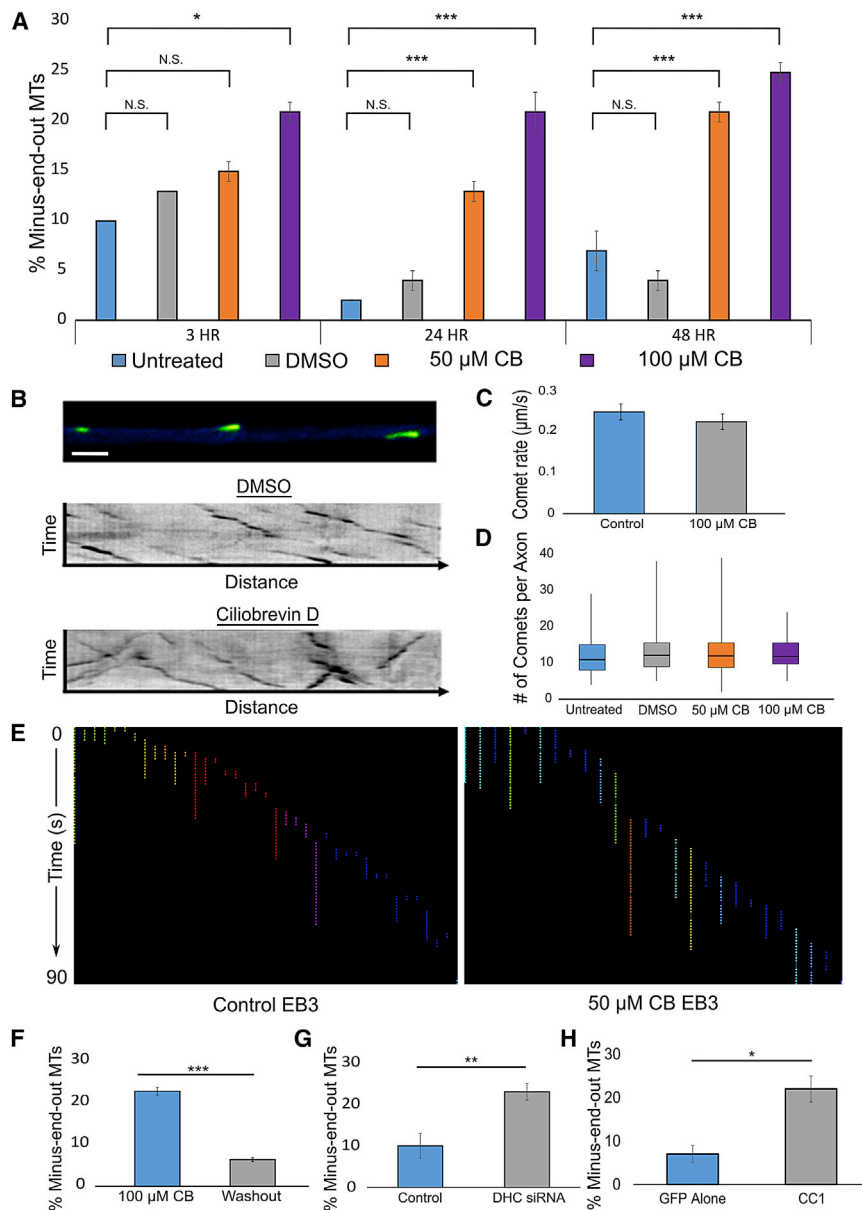


Figure 2. CB Leads to Reversible Increase in Minus-End-Out MTs in the Axon

(A) Bar graph showing the percentage of MTs oriented with minus end out in axons after 3, 24, or 48 hr of CB (at two different concentrations) or vehicle, as indicated by backward comets.

(B) Top: micrograph of GFP-EB3 forward comets, indicating plus-end-out MTs (FIJI “Green Fire” LUT; scale bar, 5 μ m). Kymographs show EB3 comets after DMSO (middle) or CB (bottom) treatment.

(C and D) Quantification of comet rate (C) and frequency (D), respectively, under control or CB conditions. No significant difference was observed.

(E) Comet track lengths quantified using the Fiji tracking plugin. Each track represents a comet run; colors are made different to increase contrast from run to run. No significant difference in run length was observed between control and CB treatment. (Washout data are in Figure S2B.)

(F) Bar graph showing the percentage of MTs oriented with minus end out (indicated by backward comets) in axons 24 hr after CB washout.

(G) Bar graph showing the percentage of MTs oriented with minus end out (indicated by backward comets) in axons after treatment with DHC siRNA.

(H) Bar graph showing the percentage of MTs oriented with minus end out (indicated by backward comets) in axons after CC1 expression.

n = 25 neurons per condition from three independent dissections. Data represent mean \pm SEM. *p < 0.05; **p < 0.01; ***p < 0.001. *p < 0.05; N.S., not significant. See also Figure S2B.

100 μ M CB or vehicle. After 3 hr, untreated and DMSO-treated neurons displayed proportions of 10% \pm 0.6% and 13% \pm 0.5% of the comets in the backward direction, while neurons treated with 50 μ M or 100 μ M CB displayed 15% \pm 1% and 21% \pm 1% of the comets in the backward direction, respectively. After 24 hr, in the case of both untreated and DMSO-treated neurons, fewer than 5% of the comets were backward. CB treatment resulted in neurons treated with 50 or 100 μ M CB exhibiting 13% \pm 1% or 21% \pm 1% backward comets, respectively. While the number of backward comets in the axon remained low for control treatments after 48 hr, backward comets increased even further in CB-treated cells, yielding 22% \pm 1% and 26% \pm 1% after 48 hr of treatment with 50 or 100 μ M CB, respectively (Figures 2A and 2B, bar graph and kymographs, respectively; Movie S1).

minus-end-out MTs from the axon (Figure 2F). DHC depletion via siRNA also yielded a significant increase in minus-end-out MTs in axons (23% \pm 4%) (Figure 2G), as did an overnight expression of CC1, a dynactin component that disrupts dynein function when expressed (Figure 2H). CC1 expression did not affect comet run length or rate (Figures S2A and S2C, respectively) and caused the appearance of axonal varicosities where MT polarity flaws were observed (Figure S2B).

MT Transport in the Axon Is Disrupted Bi-directionally with Acute Dynein Inhibition

To directly test our hypothesis about a dynein-driven, polarity-sorting mechanism (schematic in Figure 3A), live-cell imaging of MT transport was conducted over the first 5 min after washing

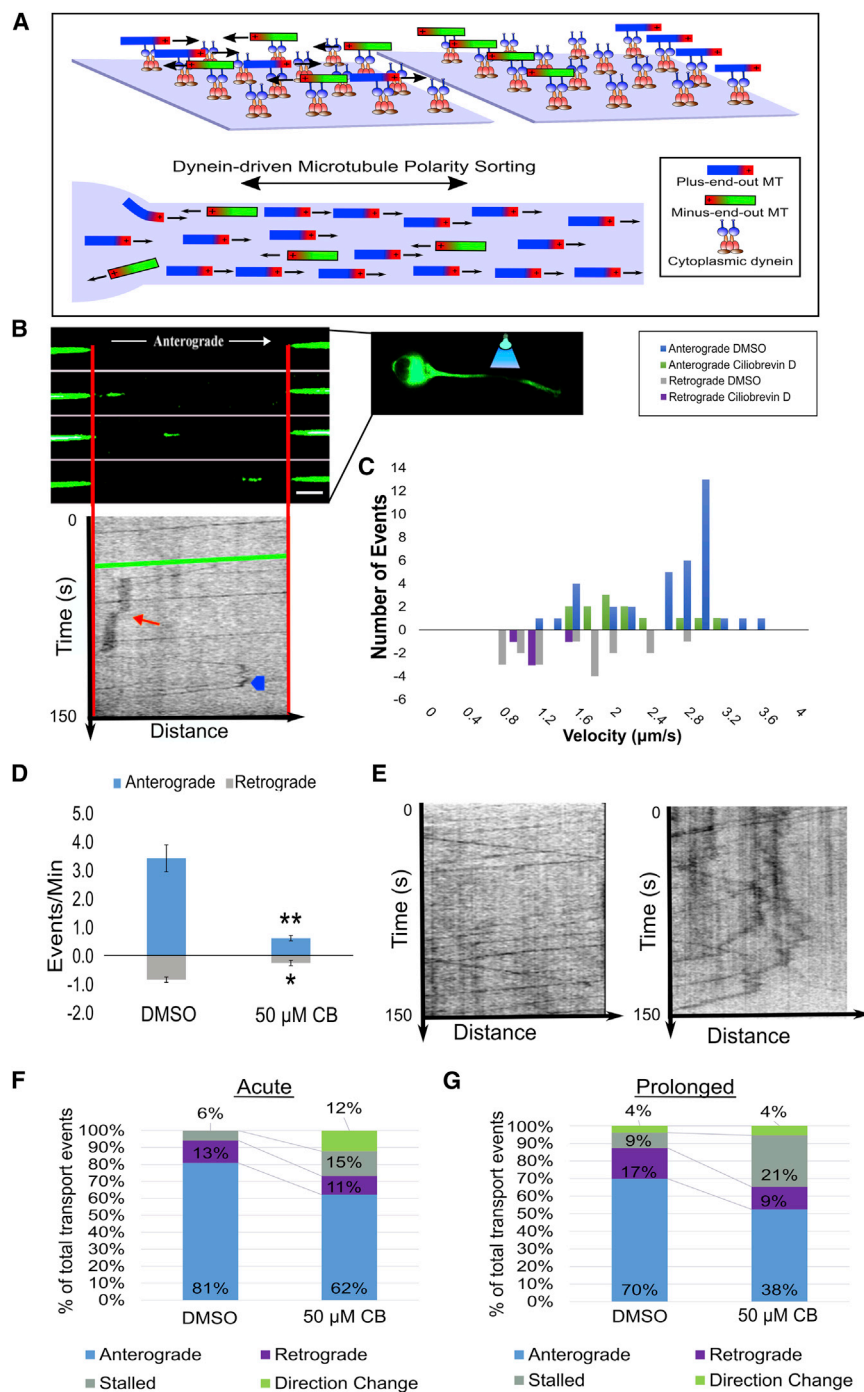


Figure 3. CB Disrupts MT Transport

(A) Schematic depicting how dynein's MT polarity-sorting ability on glass coverslips (top) is proposed to sort MTs in the axon (bottom).

(B) A representative image of a MT moving through a bleached region of an axon expressing tdEos-tubulin under control conditions (top; scale bar, 5 μ m) with an affiliated kymograph (bottom; plots position over time [150 s]). The green line represents the movement of the pictured MT. The red arrow shows a stall event, and the blue arrowhead depicts an MT reversal. Shown to the right of the time-lapse sequence is a lower magnification of the experimental neuron with a schematic illustration of a light bulb to indicate the bleaching procedure.

(C) Frequency histogram showing anterograde and retrograde transport events under DMSO and CB conditions.

(D) Bar graph showing the MT transport events per minute after CB.

(E) Kymographs (left: control; right: CB) plotting MT transport events over time (150 s).

(F and G) 100% stacked histogram of types of transport events after acute (F) and prolonged inhibition (G). Histograms show alterations in MT transport behavior after dynein inhibition when compared to DMSO control.

n = 25 neurons per condition from three independent dissections. Data represent mean \pm SEM. *p < 0.05; **p < 0.01.

the middle third of the axon (Figure 3B), and movies of transported MTs were captured first under untreated conditions and then after wash-in of either DMSO or 50 μ M CB.

The numbers of mobile MTs observed were higher than in earlier studies with GFP-tubulin (He et al., 2005), which is consistent with tdEOS-tubulin more thoroughly incorporating into MTs (Solowska et al., 2014). The identity of the mobile structures as MTs (rather than as membranous vesicles that incorporated the tdEOS-tubulin) was confirmed by treatment with FCPT, a compound that halts MT transport by inducing kinesin-5 (a motor that does not transport vesicles) to become a rigor complex (Rao et al., 2016). After FCPT wash-in, the transport of fluorescent moving structures was reduced by over 80% (Figure S3A).

In CB as well as 6 hr later on neurons expressing tubulin tagged with tdEos, a photoconvertible fluorescent label that fluoresces green until bleached, after which it fluoresces red. Compared to the GFP-tubulin used in previous studies, tdEos-tubulin allows imaging of MTs moving *through* the bleached zone in the green channel as well as *out* of the bleached zone in the red channel. Data were gathered only from the green channel for the present study. A bleached zone of approximately 30 μ m was created in

cent moving structures (and, therefore, being MTs), no diminution in the observed transport was observed in the presence of brefeldin A (Figure S3B), a drug that prevents vesicle formation (Tang et al., 2013).

Kymographs of MTs moving through the bleached zone were created, and the rate, frequency, and processivity of these

events were analyzed under control and dynein-inhibited conditions. Acute and prolonged DMSO-treated cultures showed a similar distribution of transport velocities, with the most anterograde transport events clustered between 1.5 to 3 $\mu\text{m/s}$ and retrograde transport predominantly within 1 to 2.5 $\mu\text{m/s}$ (Figure 3C). Average length of a moving MT was 3.65 μm (Figure S3C). Occasional pauses in movement were observed, as well as rare reversals in direction. Shortly after the addition of CB, a significant increase in the number of MTs that stalled or changed direction was observed, with movements in both directions diminished (Figures 3D and 3E, kymographs; Figure 3F, stacked bar graph). After prolonged CB treatment, a significant bi-directional decrease in MT transport was observed when compared to vehicle controls (Figure 3G). This was accompanied by an increase in MT stalling, but there was no difference in the number of MTs that change direction in prolonged CB-treated cultures versus control groups (Figure 3E; Movie S2).

Computational Simulations Predict that a Dynein-Based Polarity-Sorting Mechanism for Axonal MTs Requires Other Components

A dynein-based polarity-sorting model alone does not explain why only short MTs are mobile or explain the pausing and rare reversals in direction of movement. To mathematically test potential contributions of other variables, a tunable computational model of MT transport in the axon was created, using published data to inform the parameters. Stochastic simulations were used to predict the time-dependent movement of a short axonal MT oriented with plus end out. Two populations of motors, cytoplasmic dynein and a plus-end-directed kinesin, were assumed to be immobilized along the axon via cargo domain attachment to structures, including long stationary MTs and actin bundles (Hasaka et al., 2004), creating a lawn of motor proteins that stochastically attach to and detach from the short MT. When both types of motor are attached to the MT, the motors exert forces in opposite directions, creating a “tug-of-war” in which motors of the same polarity share the load force equally. Based on previous modeling and single-molecule *in vitro* experiments (Kunwar et al., 2011), linear force-velocity dependence and force-dependent detachment kinetics for individual motors were assumed. The possibility was explored of a small population of static cross-linkers that stochastically attach/detach to the MT, giving rise to viscous protein friction that opposes MT movement. The movement of the MT is determined by a force-balance condition, and the position is continually updated based on the instantaneous attachment numbers of dynein, kinesin, and cross-linkers, as described in Table S1. For minus-end-out MTs, retrograde motion with the same characteristics as those of plus-end-out MTs is predicted. Most mechanical parameters of the model, such as the stall force and detachment force for kinesin (specifically, we used data on kinesin-1, i.e., conventional kinesin) and cytoplasmic dynein, can be constrained by experimental measurements (see Table S1). We chose to vary the stochastic attachment rates of dynein, kinesin, and cross-linkers (denoted by d_{on} , k_{on} , and x_{on} , respectively) while setting all other parameters to the values listed in Table S1, in order to probe model predictions for the role played by each of these proteins in axonal MT transport. The attachment rate of each protein is in-

tended to encompass the binding affinity of each protein to MTs as well as the unknown density of each protein in the axon.

When $d_{\text{on}} \gg k_{\text{on}}$, making dynein the primary driver of motion, the model predicts sorting of MTs based on their polarity orientation (Figure 4A). When the MT is transported by dynein alone ($d_{\text{on}} = 0.1 \text{ s}^{-1}$, and $k_{\text{on}} = x_{\text{on}} = 0$), fast and processive anterograde MT transport is predicted (Figure 4A, blue line). Adding the activity of a kinesin motor ($d_{\text{on}} = 0.1 \text{ s}^{-1}$, $k_{\text{on}}/d_{\text{on}} = 0.1$, and $x_{\text{on}} = 0$) (Figure 4A, red line) or kinesin and static cross-linkers along with dynein ($d_{\text{on}} = 0.1 \text{ s}^{-1}$, $k_{\text{on}}/d_{\text{on}} = 0.1$, and $x_{\text{on}} = 0.003 \text{ s}^{-1}$) (Figure 4A, green line) produces saltatory transport reminiscent of the experimental observations.

The time-averaged velocity (including pauses) of a plus-end-out MT was simulated as a function of MT length for several values of kinesin attachment rate and static cross-linker binding rate (Figure 4B). In the absence of static cross-linkers, the average velocity of MT transport increases with MT length, contrasting with the experimental observation that only short MTs are motile in the axon. With the addition of static cross-linkers, which create an effective viscous drag force opposing the motion of the MT, the average velocity decreases with MT length, in agreement with experimental observations. This is because static cross-linkers increase the likelihood of a stalled tug-of-war between dynein and kinesin by reducing the force on each kinesin motor, thus decreasing detachment rate and increasing the average kinesin attachment number (Figure 4C).

The model predicts that, if dynein activity level is reduced (for example, by CB), the small level of pre-existing kinesin activity begins to play a larger role in MT transport, reversing the direction of motion for very low levels of dynein activity (Figures 4D and 4E). For intermediate levels of dynein activity, competition between dynein and kinesin leads to frequent reversals of motion (Figure 4D, inset). The model predicts that a small reduction in dynein activity will initially increase the fraction of time spent paused in a stalled tug-of-war but also that the fraction of time spent paused is insensitive to further reduction in dynein activity (Figure 4E). MT transport becomes independent of MT polarity for intermediate levels of dynein activity ($k_{\text{on}}/d_{\text{on}}$, $\sim 0.2\text{--}0.5$), thus disrupting the polarity-sorting mechanism that exists when dynein is the primary driver of motion ($k_{\text{on}}/d_{\text{on}} < 0.1$) (Figure 4E). By tuning the activity levels of dynein and kinesin, the model can account for disorganized MT transport and corruption of MT polarity patterns that occurs when dynein activity in the axon is inhibited.

Partial Depletion of TRIM46, an Axonal MT Cross-Linker, Leads to an Increase in MT Transport and an Accumulation of MTs in the Distal Axon

TRIM46, a protein that is normally enriched proximally in the axon, is an attractive candidate for the cross-linker predicted by our modeling, because its depletion leads to MT polarity flaws in the axon (van Beuningen et al., 2015). TRIM46 siRNA (or control siRNA) was introduced into neurons at the time of plating, and cells were fixed after 26–30 hr. Most TRIM46 was observed in the soma and proximal axon but along the length of the axon as well. Neurons treated with TRIM46 siRNA exhibited a $38\% \pm 4\%$ reduction in TRIM46 immunofluorescence signal when compared to control siRNA (Figures S4A–S4C, bar graph), and

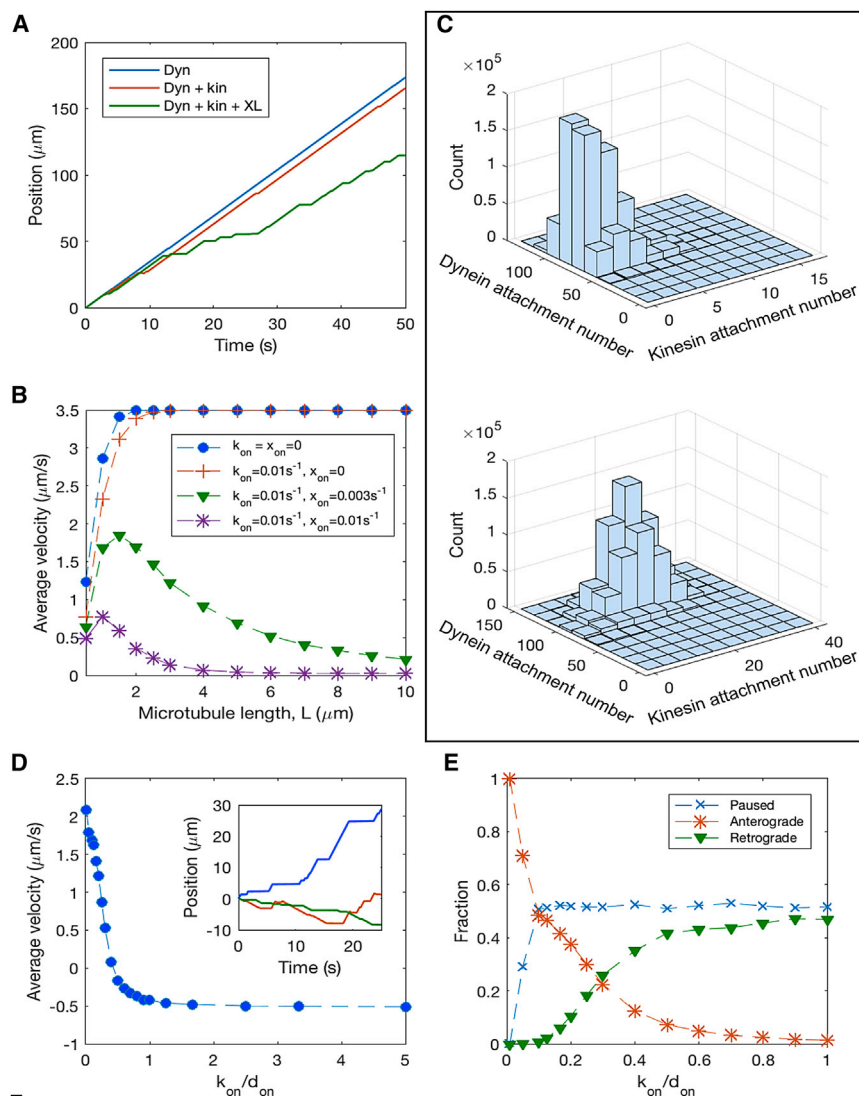


Figure 4. Computational Simulations of MT Transport Predict that Dynein-Driven MT Transport Establishes the Axonal MT Polarity Pattern

(A) Position as a function of time for an individual MT of length, $L = 2 \mu\text{m}$ with plus end out, showing sample trajectories in the presence of dynein only (Dyn; $d_{\text{on}} = 0.1 \text{ s}^{-1}$, and $k_{\text{on}} = x_{\text{on}} = 0$; blue line); dynein and kinesin activity (Dyn + kin; $d_{\text{on}} = 0.1 \text{ s}^{-1}$, and $k_{\text{on}} = 0.01 \text{ s}^{-1}$; red line); and dynein, kinesin, and static cross-linkers (Dyn + kin + XL; $d_{\text{on}} = 0.1 \text{ s}^{-1}$, $k_{\text{on}} = 0.01 \text{ s}^{-1}$, and $x_{\text{on}} = 0.003 \text{ s}^{-1}$; green line).

(B) Time-averaged velocity (including pauses) of an MT with plus end out as a function of MT length, for several values of kinesin binding rate and static cross-linker binding rate.

(C) Top: histogram of dynein and kinesin attachment numbers in the absence of static cross-linkers ($L = 10 \mu\text{m}$; $d_{\text{on}} = 0.1 \text{ s}^{-1}$, $k_{\text{on}}/d_{\text{on}} = 0.1$, and $x_{\text{on}} = 0$). Bottom: histogram of dynein and kinesin attachment numbers in the presence of static cross-linkers ($L = 10 \mu\text{m}$; $d_{\text{on}} = 0.1 \text{ s}^{-1}$, $k_{\text{on}}/d_{\text{on}} = 0.1$, and $x_{\text{on}} = 0.003 \text{ s}^{-1}$).

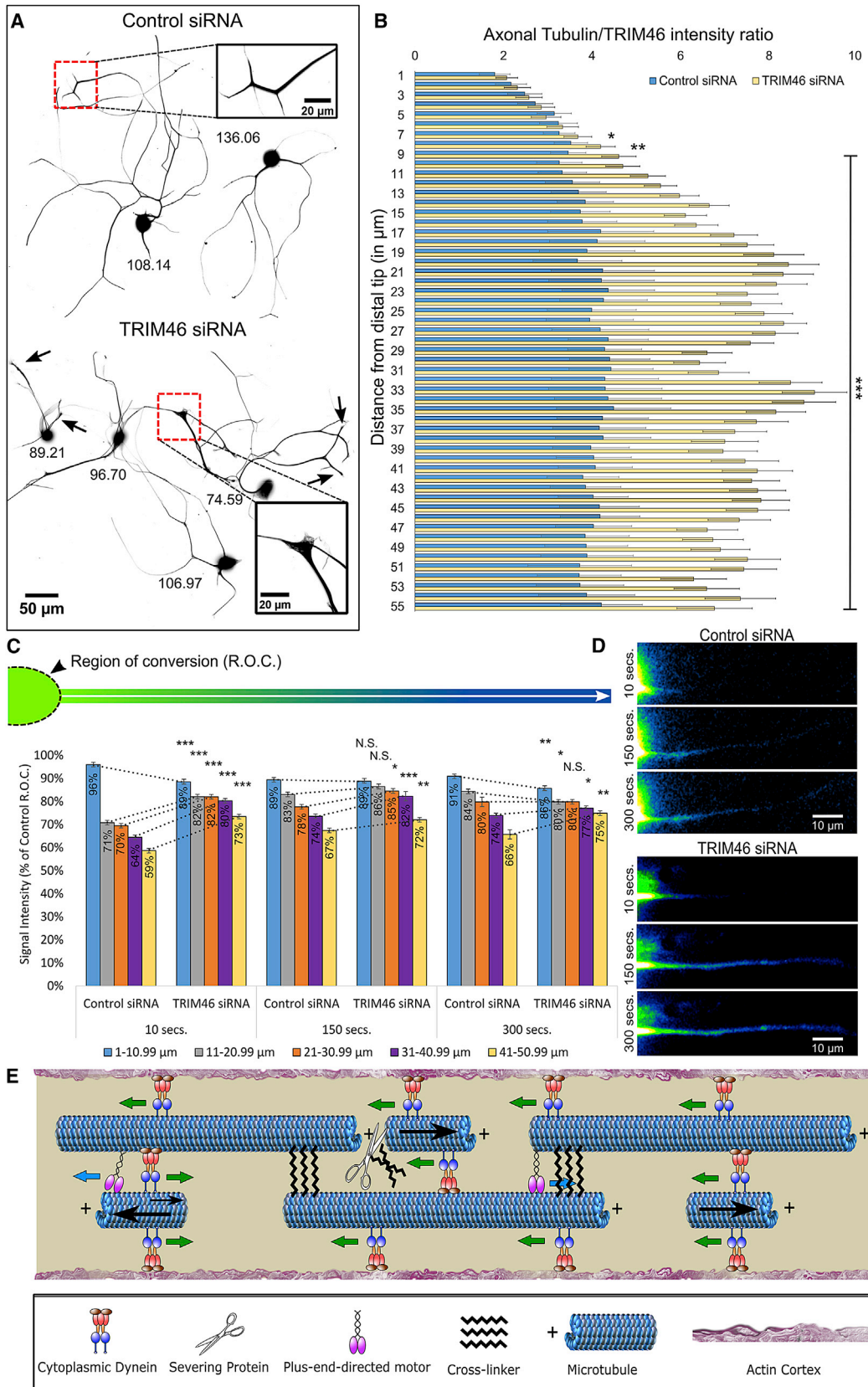
(D) Average velocity as a function of $k_{\text{on}}/d_{\text{on}}$, for $L = 2 \mu\text{m}$; $k_{\text{on}} = 0.01 \text{ s}^{-1}$, and $x_{\text{on}} = 0.003 \text{ s}^{-1}$. Inset: illustrative MT trajectories corresponding to $k_{\text{on}}/d_{\text{on}} = 0.1$ (blue), $k_{\text{on}}/d_{\text{on}} = 0.5$ (red), and $k_{\text{on}}/d_{\text{on}} = 1$ (green).

(E) Fraction of time spent paused, moving anterogradely, and moving retrogradely as a function of $k_{\text{on}}/d_{\text{on}}$. The dashed lines between data points in (B), (D), and (E) are included as a guide to the eye.

reduction in TRIM46 was significantly correlated with severity of the swollen distal tip phenotype (Figure S4C, scatterplot). Relative to control axons, the proximal enrichment of TRIM46 was diminished or entirely lost after partial depletion of the protein, with the distal-to-proximal proportion of TRIM46 notably higher (Figures 5A and 5B; Figures S4A and S4B, inset). We speculate that the distribution of TRIM46 along the axon is a reflection of the degree to which it is able to restrain MT transport, with its redistribution after partial depletion indicating its diminished capacity to impede the transport of MTs to which it is bound. Consistent with this speculation, distal axons displayed an abnormal accumulation of MTs, and the tips of these axons were wider and blunter than those of control axons, presumably as a result of the MT accumulation.

If TRIM46 is the hypothetical cross-linker predicated by our model, the distal accumulation of MTs after TRIM46 depletion would presumably result from greater sliding of MTs, both long and short ones. Because movement of long MTs is not easily

visualized in the axon, we used a modification of our live-cell regimen recently used to appreciate the sliding of longer MTs in the leading process of migratory neurons (Rao et al., 2016). For this, we expressed tEOS-tubulin and converted the soma and the proximal region of the axon from green to red. We then measured the appearance of red signal at three time points (10, 150, and 300 s) in the non-converted region of the axon as an indication of the sliding of MTs into that region from the converted region. Imaging was performed just 2 hr after the addition of laminin, prior to the distal accumulation of MTs, so that we could determine whether an increase in MT transport could account for the subsequent MT accumulation. Cells treated with control siRNA showed modest red fluorescence signal appearing over time in the unconverted region of the axon (Figures 5C and 5D [shown in the Fiji “Green Fire” Look Up Table; LUT]; Figure S4D), which may be due to some MT sliding but also some incorporation of converted tubulin subunits into non-moving long MTs. The levels of red fluorescence appearing in the non-converted region was notably greater in cells partially depleted of TRIM46 (Figures 5C, S4E, and S4F; Movie S3), to which we attribute greater MT sliding, as TRIM46 does not affect MT dynamics (van Beuningen et al., 2015). These results, more details of which are described in



(legend on next page)

the figure legends, indicate increased sliding of MTs when TRIM46 is depleted.

DISCUSSION

In support of a dynein-based, polarity-sorting mechanism for organizing MTs in the axon, our studies show a strong positive correlation between the experimental inhibition of dynein-driven transport of MTs and the accumulation in the axon of minus-end-out MTs. Our data indicating that dynein transports MTs in both directions in the axon contrast with the results of recent studies on cultured *Drosophila* neurons, in which dynein was implicated only in the retrograde transport of minus-end-out MTs (del Castillo et al., 2015; Zheng et al., 2008). Instead, evidence was presented in that work that kinesin-1 slides antiparallel MTs in the cell body and at the axon tip to drive axon outgrowth. Perhaps relevant to this apparent conflict is a recent paper on vertebrate muscle cells in which MT sliding was shown to occur via dynein but could occur via kinesin-1 if dynein were depleted (Mogessie et al., 2015). Consistent with that finding, our computational modeling suggests that dynein will dominate kinesin-1 when the two directly compete to slide MTs, at least at the predicted physiological levels of the two motors. Individual MTs moving within vertebrate axons occasionally pause, and even (albeit rarely) reverse direction, suggesting an opposing force on the MTs. Kinesin-1 seems like a good candidate for an opposing motor and also makes sense as the motor that aberrantly transports MTs in the axon when dynein is depleted. As suggested by the insect work (Lu et al., 2015) and recent work in zebrafish (Lee et al., 2017), we suspect that there are particular events in the life of the axon, such as growth-related challenges at the axon tip and the formation of axonal branches, that could benefit from the forces of anti-parallel MT sliding by kinesin-1.

Our computational modeling also predicts the participation of a cross-linker protein that would limit concerted transport of MTs to those that are very short and also tamp down uncontrolled MT movements. The precedent for such a cross-linker comes from the work on muscle cells mentioned earlier, in which an isoform of MAP4 strongly influences the capacity of motors to slide MTs (Mogessie et al., 2015). To test the principle in axons, we chose TRIM46 as an appealing candidate, because it has already been

shown to be relevant to the polarity orientation of axonal MTs (van Beuningen et al., 2015). We speculate that MT polarity flaws arise in the axon when TRIM46 is depleted, because MT movements become insufficiently controlled (Figure 5E). In support of such a scenario, partial depletion of TRIM46 in our experiments resulted in dramatically greater sliding of MTs, no longer limited to just the shortest MTs in the axon and, we suspect, no longer limited to just dynein.

An obvious question is: how do vertebrate dendrites overcome dynein-based polarity-sorting forces to generate and maintain MT arrays of mixed orientation (Baas et al., 1988; Yau et al., 2016): One possibility is that local MT nucleation events occur in dendrites, via gamma-tubulin and Golgi outposts that introduce minus-end-out MTs (Nguyen et al., 2014; Delandre et al., 2016). This is probably not the primary mechanism however, because the presence of Golgi elements in dendrites requires that at least some minus-end-out MTs are already present (Baas et al., 1988). In keeping with a motor-based mechanism for organizing neuronal MTs, we have proposed that certain kinesins, best known for their roles in mitosis, transport minus-end-out MTs into developing dendrites (Baas, 1999) and then hold them there in opposition to dynein's polarity-sorting properties. If these kinesins are depleted, the minus-end-out MTs are chased back into the cell body, and the dendrite reverts to an axonal identity (Yu et al., 2000). These kinesins diminish in expression in adult neurons (Lin et al., 2012); hence, the mixed orientation of dendritic MTs presumably requires other factors, such as cross-linker proteins, to oppose the polarity-sorting properties of dynein over the life of the neuron.

EXPERIMENTAL PROCEDURES

Cell Culture

SCGs were cultured as previously described (He et al., 2005) from newborn rat pups, following procedures approved by the Institutional Animal Care and Use Committee at Drexel University.

Live-Cell Imaging

For MT orientation experiments: neurons expressing GFP-EB3, a +tip that affiliates with the plus end of MTs during bouts of assembly, were treated with 50 μ M CB, 100 μ M CB, or vehicle (DMSO). The excursion of GFP-EB3 at the plus end of the MT appears as a "comet," with forward and backward

Figure 5. TRIM46 Depletion Results in Redistribution of Axonal MTs and an Increase in MT Transport

(A) SCG neurons immunostained for beta-tubulin and TRIM46, with only the beta-tubulin staining shown. Image is inverted to increase contrast. Top: neurons treated with control siRNA. Bottom: neurons treated with TRIM46 siRNA. Arrows indicate abnormally blunted tips of TRIM46-depleted axons; inset boxes show distal axons magnified. Numerals in black represent TRIM46 immunofluorescence gray value (for immunostain images of TRIM46, see Figures S4A and S4B). (B) Bar graph depicting the tubulin:TRIM46 ratio in the distal region of the axon (26–28 hr after TRIM46 depletion), indicating a change from (as a result of partial TRIM46 depletion) the predominantly proximal enrichment of TRIM46 to a relatively higher proportion of the remaining TRIM46 (relative to tubulin staining) in the distal region of the axon where MTs accumulate during TRIM46 depletion. (C) Bar graph depicting the tdEos-tubulin signal intensity (red fluorescence after conversion from green to red) as percentage of control across distances (five 10- μ m groups; 1–10.99, 11–20.99, 21–30.99, 31–40.99, and 41–50.99) at 10 s, 150 s, and 300 s post-conversion. Relative to control, a greater amount of fluorescence recovery occurs in regions beyond the conversion zone in TRIM46-depleted axons, indicating greater levels of MT sliding (see Rao et al., 2016). (D) Representative live-cell-imaging frames of control and TRIM46-siRNA-treated neurons expressing tdEos-tubulin, shown in the Fiji "Green Fire" LUT. (E) Schematic displays proposed a dynein-based, polarity-sorting mechanism for generating and preserving the plus-end-out orientation of MTs in the axon. The proposed mechanism involves cytoplasmic dynein as the polarity-sorting motor but also as a plus-end-directed kinesin motor and a cross-linker protein. Blue arrows indicate direction of kinesin. Green arrows indicate direction of dynein. Black arrows indicate MT movement, with varying size representing directional force.

n = 15 neurons per condition from three independent dissections. Data represent mean \pm SEM. *p < 0.05; **p < 0.01; ***p < 0.001; N.S., not significant. See also Figures S4A and S4B.

excursions indicating plus-end-out and minus-end-out MTs, respectively (Hakasa et al., 2004). SCGs were harvested as described earlier, dissociated, and transfected with GFP-EB3 by nucleofection prior to plating on poly-D-lysine (PDL) without laminin. 12 hr after plating, the medium was replaced with medium containing laminin (10 μ g/mL) and treatment compounds (no compound, DMSO, 50 μ M CB, or 100 μ M CB). Dishes were then placed in the live-cell imaging workstation (5% CO₂, 37°C), and neurons from five randomly selected regions of the dish were chosen for imaging at 3-hr, 24-hr, and 48-hr time points. Images were captured at two frames per second (fps) using a Zeiss 200M Axiovert microscope equipped with a Zeiss Neofluar 100 \times objective (NA, 1.3). For MT transport experiments: cells were transfected with tdEOS-tubulin prior to plating. 12 hr after plating on PDL/laminin, dishes were placed in a live-cell-imaging workstation, and neurons from five randomly selected regions were imaged. A bleached zone of approximately 30 μ m was made in the middle third of the imaged axon using the Andor Mosaic system, and images were captured every 500 ms using a Zeiss AxioObserver Z1 equipped with a 100 \times Plan Apochromat oil objective (NA, 1.46). For TRIM46 transport: 20 hr after TRIM46 siRNA treatment, somal tdEOS-tubulin was converted, and the axon was imaged every 5 s for 2.5 min. For vesicle transport assay: neurons were incubated overnight in medium containing rhodamine-labeled dextran conjugates (1 mg/mL). The following day, dextran medium was removed, and neurons were washed twice with dextran-free medium and imaged, first under control conditions and then after wash-in of treatments (DMSO, 50 μ M CB, or 100 μ M CB).

Fluorescence Microscopy on Fixed Cultures

For axon length analysis: neurons treated with DMSO, 50 μ M CB, or 100 μ M CB were fixed 3 hr after plating on 0.1 mg/mL PDL with laminin and immunostained for β 3-tubulin. Images were taken using a Zeiss Axiovert 200M inverted microscope equipped with a Zeiss 40 \times oil objective (NA, 1.2), and image acquisition was controlled using the Zeiss Zen Blue software. Images used for quantification did not contain pixel saturation and showed minimal bleaching during imaging acquisition. For growth cone analysis: for experiments quantifying the number of filopodia containing MTs, neurons were treated and fixed as described earlier and immunostained for β 3-tubulin and actin. Images were taken using a Zeiss Axiovert 200M inverted microscope equipped with a Zeiss 100 \times oil objective (NA, 1.3). For Golgi analysis: neurons were plated on glass-bottomed dishes coated with PDL and laminin and fixed with methanol after 3 hr. Cultures were stained for tubulin and for Golgi using an anti-Golgi 58K antibody and imaged by epifluorescence. For neurofilament analysis: distribution of neurofilaments was ascertained according to our previous method (He et al., 2005). For DHC and CC1 expression: EB3 comet movies were obtained from DHC siRNA studies conducted as previously described (Myers et al., 2006), with the siRNA pool consisting of four non-overlapping sequences that individually produced the same result as each of the four on its own, providing confidence in the specificity of the phenotype (Supplemental Experimental Procedures; He et al., 2005). As another method for inhibiting dynein function, a fluorescently tagged CC1 construct was expressed in cells for 24 hr (Supplemental Experimental Procedures); expression of CC1 disrupts the dynein complex and thereby inhibits dynein functions (Quintyne et al., 1999). For TRIM46 depletion: four pooled non-overlapping sequences of TRIM46 siRNA were introduced by nucleofection.

All images were acquired at identical exposure settings. Images used for quantification did not contain pixel saturation and showed minimal bleaching during imaging acquisition.

Data Analyses and Statistics

Data represent, if not otherwise specified, mean \pm SEM. In each experiment, three independent repeats were performed. The MT transport, EB3 comet, and vesicle transport assays were performed using the Zeiss Zen Blue software package. Axon length measurements, growth cone analyses, vesicle transport, EB3 comet analyses, and MT transport analyses were performed using publicly available, open-source plugins in Fiji. Analyses were performed by a blinded rater. All statistical analyses were performed using SPSS 23 (IBM), and graphs were constructed using Microsoft Excel. Multiple group comparison was performed by one-way ANOVA followed by Bonferroni post hoc analyses. Student's t test was used for pair analyses.

Computational Modeling

The time-dependent trajectory of an individual MT transported along the axon was simulated by a sliding filament mechanism. The instantaneous velocity of the MT was determined by a force-balance condition, in which the force acting on the MT is determined by the instantaneous attachment numbers of dynein, N_d; kinesin-1, N_k; and static cross-linkers, N_x.

SUPPLEMENTAL INFORMATION

Supplemental Information includes Supplemental Experimental Procedures, four figures, one table, and three movies and can be found with this article online at <http://dx.doi.org/10.1016/j.celrep.2017.05.064>.

AUTHOR CONTRIBUTIONS

A.N.R. conducted most of the experiments. A.P. and K.A.M. each conducted a relatively smaller number of experiments. E.M.C. and H.T.Y. did the modeling. M.M.B. helped interpret data. P.W.B. led the project and worked with A.N.R. to design the experiments and write the manuscript.

ACKNOWLEDGMENTS

This work was supported by a grant to P.W.B. from the National Institute of Neurological Disorders and Stroke (NINDS) (R01 NS28785). A.N.R. is supported by an NRSA (F31 NS093748) from the NINDS. For tools and advice, we thank Timothy Mitchison of Harvard University and Erika Holzbaur of University of Pennsylvania.

Received: October 3, 2016

Revised: April 20, 2017

Accepted: May 18, 2017

Published: June 13, 2017

REFERENCES

- Ahmad, F.J., Echeverri, C.J., Vallee, R.B., and Baas, P.W. (1998). Cytoplasmic dynein and dynactin are required for the transport of microtubules into the axon. *J. Cell Biol.* 140, 391–401.
- Ahmad, F.J., He, Y., Myers, K.A., Hasaka, T.P., Francis, F., Black, M.M., and Baas, P.W. (2006). Effects of dynactin disruption and dynein depletion on axonal microtubules. *Traffic* 7, 524–537.
- Arthur, A.L., Yang, S.Z., Abellaneda, A.M., and Wildonger, J. (2015). Dendrite arborization requires the dynein cofactor NudE. *J. Cell Sci.* 128, 2191–2201.
- Baas, P.W. (1999). Microtubules and neuronal polarity: lessons from mitosis. *Neuron* 22, 23–31.
- Baas, P.W., and Ahmad, F.J. (1992). The plus ends of stable microtubules are the exclusive nucleating structures for microtubules in the axon. *J. Cell Biol.* 116, 1231–1241.
- Baas, P.W., and Mozgova, O.I. (2012). A novel role for retrograde transport of microtubules in the axon. *Cytoskeleton* 69, 416–425.
- Baas, P.W., Deitch, J.S., Black, M.M., and Banker, G.A. (1988). Polarity orientation of microtubules in hippocampal neurons: uniformity in the axon and nonuniformity in the dendrite. *Proc. Natl. Acad. Sci. USA* 85, 8335–8339.
- del Castillo, U., Winding, M., Lu, W., and Gelfand, V.I. (2015). Interplay between kinesin-1 and cortical dynein during axonal outgrowth and microtubule organization in *Drosophila* neurons. *eLife* 4, e10140.
- Delandre, C., Amikura, R., and Moore, A.W. (2016). Microtubule nucleation and organization in dendrites. *Cell Cycle* 15, 1685–1692.
- Dillman, J.F., 3rd, Dabney, L.P., Karki, S., Paschal, B.M., Holzbaur, E.L., and Pfister, K.K. (1996). Functional analysis of dynactin and cytoplasmic dynein in slow axonal transport. *J. Neurosci.* 16, 6742–6752.
- Firestone, A.J., Weinger, J.S., Maldonado, M., Barlan, K., Langston, L.D., O'Donnell, M., Gelfand, V.I., Kapoor, T.M., and Chen, J.K. (2012).

- Small-molecule inhibitors of the AAA+ ATPase motor cytoplasmic dynein. *Nature* 484, 125–129.
- Hasaka, T.P., Myers, K.A., and Baas, P.W. (2004). Role of actin filaments in the axonal transport of microtubules. *J. Neurosci.* 24, 11291–11301.
- He, Y., Francis, F., Myers, K.A., Yu, W., Black, M.M., and Baas, P.W. (2005). Role of cytoplasmic dynein in the axonal transport of microtubules and neurofilaments. *J. Cell Biol.* 168, 697–703.
- Heidemann, S.R., Landers, J.M., and Hamborg, M.A. (1981). Polarity orientation of axonal microtubules. *J. Cell Biol.* 91, 661–665.
- Kunwar, A., Tripathy, S.K., Xu, J., Mattson, M.K., Anand, P., Sigua, R., Vershinin, M., McKenney, R.J., Yu, C.C., Mogilner, A., and Gross, S.P. (2011). Mechanical stochastic tug-of-war models cannot explain bidirectional lipid droplet transport. *Proc Natl Acad Sci USA* 108, 18960–18965.
- Lee, T.J., Lee, J.W., Haynes, E.M., Eliceiri, K.W., and Halloran, M.C. (2017). The kinesin adaptor Calsyntenin-1 organizes microtubule polarity and regulates dynamics during sensory axon arbor development. *Front. Cell. Neurosci.* 11, 107.
- Lin, S., Liu, M., Mozgova, O.I., Yu, W., and Baas, P.W. (2012). Mitotic motors coregulate microtubule patterns in axons and dendrites. *J. Neurosci.* 32, 14033–14049.
- Lu, W., Lakonishok, M., and Gelfand, V.I. (2015). Kinesin-1-powered microtubule sliding initiates axonal regeneration in *Drosophila* cultured neurons. *Mol. Biol. Cell* 26, 1296–1307.
- Mogessie, B., Roth, D., Rahil, Z., and Straube, A. (2015). A novel isoform of MAP4 organizes the paraxial microtubule array required for muscle cell differentiation. *eLife* 4, e05697.
- Myers, K.A., Tint, I., Nadar, C.V., He, Y., Black, M.M., and Baas, P.W. (2006). Antagonistic forces generated by cytoplasmic dynein and myosin-II during growth cone turning and axonal retraction. *Traffic* 7, 1333–1351.
- Nguyen, M.M., McCracken, C.J., Milner, E.S., Goetschius, D.J., Weiner, A.T., Long, M.K., Michael, N.L., Munro, S., and Rolls, M.M. (2014). γ -tubulin controls neuronal microtubule polarity independently of Golgi outposts. *Mol. Biol. Cell* 25, 2039–2050.
- Qiang, L., Yu, W., Liu, M., Solowska, J.M., and Baas, P.W. (2010). Basic fibroblast growth factor elicits formation of interstitial axonal branches via enhanced severing of microtubules. *Mol. Biol. Cell* 21, 334–344.
- Quintyne, N.J., Gill, S.R., Eckley, D.M., Crego, C.L., Compton, D.A., and Schroer, T.A. (1999). Dynactin is required for microtubule anchoring at centrosomes. *J. Cell Biol.* 147, 321–334.
- Rao, A.N., Falnikar, A., O'Toole, E.T., Mophew, M.K., Hoenger, A., Davidson, M.W., Yuan, X., and Baas, P.W. (2016). Sliding of centrosome-unattached microtubules defines key features of neuronal phenotype. *J. Cell Biol.* 213, 329–341.
- Roossien, D.H., Lamoureux, P., and Miller, K.E. (2014). Cytoplasmic dynein pushes the cytoskeletal meshwork forward during axonal elongation. *J. Cell Sci.* 127, 3593–3602.
- Sainath, R., and Gallo, G. (2015). The dynein inhibitor Ciliobrevin D inhibits the bidirectional transport of organelles along sensory axons and impairs NGF-mediated regulation of growth cones and axon branches. *Dev. Neurobiol.* 75, 757–777.
- Sánchez-Huertas, C., Freixo, F., Vlais, R., Lacasa, C., Soriano, E., and Lüders, J. (2016). Non-centrosomal nucleation mediated by augmin organizes microtubules in post-mitotic neurons and controls axonal microtubule polarity. *Nat. Commun.* 7, 12187.
- Solowska, J.M., D'Rozario, M., Jean, D.C., Davidson, M.W., Marena, D.R., and Baas, P.W. (2014). Pathogenic mutation of spastin has gain-of-function effects on microtubule dynamics. *J. Neurosci.* 34, 1856–1867.
- Tanenbaum, M.E., Vale, R.D., and McKenney, R.J. (2013). Cytoplasmic dynein crosslinks and slides anti-parallel microtubules using its two motor domains. *eLife* 2, e00943.
- Tang, Y., Scott, D., Das, U., Gitler, D., Ganguly, A., and Roy, S. (2013). Fast vesicle transport is required for the slow axonal transport of synapsin. *J. Neurosci.* 33, 15362–15375.
- van Beuningen, S.F., Will, L., Harterink, M., Chazeau, A., van Battum, E.Y., Frias, C.P., Franker, M.A., Katrukha, E.A., Stucchi, R., Vocking, K., et al. (2015). TRIM46 controls neuronal polarity and axon specification by driving the formation of parallel microtubule arrays. *Neuron* 88, 1208–1226.
- Yau, K.W., van Beuningen, S.F., Cunha-Ferreira, I., Cloin, B.M., van Battum, E.Y., Will, L., Schätzle, P., Tas, R.P., van Krugten, J., Katrukha, E.A., et al. (2014). Microtubule minus-end binding protein CAMSAP2 controls axon specification and dendrite development. *Neuron* 82, 1058–1073.
- Yau, K.W., Schätzle, P., Tortosa, E., Pagès, S., Holtmaat, A., Kapitein, L.C., and Hoogenraad, C.C. (2016). Dendrites in vitro and in vivo contain microtubules of opposite polarity and axon formation correlates with uniform plus-end-out microtubule orientation. *J. Neurosci.* 36, 1071–1085.
- Yu, W., Cook, C., Sauter, C., Kuriyama, R., Kaplan, P.L., and Baas, P.W. (2000). Depletion of a microtubule-associated motor protein induces the loss of dendritic identity. *J. Neurosci.* 20, 5782–5791.
- Zheng, Y., Wildonger, J., Ye, B., Zhang, Y., Kita, A., Younger, S.H., Zimmerman, S., Jan, L.Y., and Jan, Y.N. (2008). Dynein is required for polarized dendritic transport and uniform microtubule orientation in axons. *Nat. Cell Biol.* 10, 1172–1180.